

Constraining CMB temperature evolution with Sunyaev-Zel'dovich galaxy clusters from the Atacama Cosmology Telescope

YUNYANG LI (李云炀)  ¹, ADAM D. HINCKS  ², STEFANIA AMODEO  ³, ELIA S. BATTISTELLI  ⁴, J. RICHARD BOND  ⁵, ERMINIA CALABRESE, ⁶ MARK J. DEVLIN, ⁷ JO DUNKLEY  ^{8,9}, SIMONE FERRARO  ^{10,11}, VERA GLUSCEVIC, ¹², YILUN GUAN  ¹³, MARK HALPERN, ¹⁴ MATT HILTON  ^{15,16}, RENEE HLOZEK  ^{2,17}, TOBIAS A. MARRIAGE  ¹, JEFF McMAHON, ^{18,19,20,21,22} KAVILAN MOODLEY, ^{15,16} SIGURD NAESS  ²³, FEDERICO NATI  ²⁴, MICHAEL D. NIEMACK, ^{25,3} JOHN ORLOWSKI-SCHERER  ⁷, LYMAN PAGE  ⁸, BRUCE PARTRIDGE  ²⁶, MARIA SALATINO, ^{27,28}, EMMANUEL SCHAAN  ^{10,11}, ALESSANDRO SCHILLACI, ²⁹ NEELIMA SEHGAL, ³⁰ CRISTÓBAL SIFÓN  ³¹, SUZANNE T. STAGGS, ⁸ ALEXANDER VAN ENGELEN, ³² EDWARD J. WOLACK  ³³, AND ZHILEI XU  ^{7,34}

¹ Department of Physics and Astronomy, Johns Hopkins University, 3701 San Martin Drive, Baltimore, MD 21218, USA

² David A. Dunlap Department of Astronomy & Astrophysics, University of Toronto, 50 St. George St., Toronto, ON M5S 3H4, Canada

³ Department of Astronomy, Cornell University, Ithaca, NY 14853, USA

⁴ Sapienza—University of Rome—Physics department, Piazzale Aldo Moro 5—I-00185, Rome, Italy

⁵ Canadian Institute for Theoretical Astrophysics, University of Toronto, 60 St. George St., Toronto, ON M5S 3H8, Canada

⁶ School of Physics and Astronomy, Cardiff University, The Parade, Cardiff, Wales, CF24 3AA, UK

⁷ Department of Physics and Astronomy, University of Pennsylvania, 209 South 33rd Street, Philadelphia, PA 19104, USA

⁸ Joseph Henry Laboratories of Physics, Jadwin Hall, Princeton University, Princeton, NJ 08544, USA

⁹ Department of Astrophysical Sciences, Princeton University, Peyton Hall, Princeton, NJ 08544, USA

¹⁰ Lawrence Berkeley National Laboratory, One Cyclotron Road, Berkeley, CA 94720, USA

¹¹ Berkeley Center for Cosmological Physics, UC Berkeley, CA 94720, USA

¹² Department of Physics and Astronomy, University of Southern California, Los Angeles, CA 90089, USA

¹³ Department of Physics and Astronomy, University of Pittsburgh, Pittsburgh, PA 15260, USA

¹⁴ Department of Physics and Astronomy, University of British Columbia, Vancouver, BC, V6T 1Z4, Canada

¹⁵ Astrophysics Research Centre, University of KwaZulu-Natal, Westville Campus, Durban 4041, South Africa

¹⁶ School of Mathematics, Statistics & Computer Science, University of KwaZulu-Natal, Westville Campus, Durban 4041, South Africa

¹⁷ Dunlap Institute for Astronomy and Astrophysics, University of Toronto, 50 St. George St., Toronto, ON M5S 3H4, Canada

¹⁸ Kavli Institute for Cosmological Physics, University of Chicago, Chicago, IL 60637, USA

¹⁹ Department of Astronomy and Astrophysics, University of Chicago, 5640 S. Ellis Ave., Chicago, IL 60637, USA

²⁰ Department of Physics, University of Chicago, Chicago, IL 60637, USA

²¹ Enrico Fermi Institute, University of Chicago, Chicago, IL 60637, USA

²² Department of Physics, University of Michigan, Ann Arbor, MI 48109, USA

²³ Center for Computational Astrophysics, Flatiron Institute, New York, NY 10010, USA

²⁴ Department of Physics, University of Milano-Bicocca, Piazza della Scienza 3, 20126 Milano (MI), Italy

²⁵ Department of Physics, Cornell University, Ithaca, NY 14853, USA

²⁶ Department of Physics and Astronomy, Haverford College, Haverford, PA 19041, USA

²⁷ Physics Department Stanford University, Stanford, CA 94305, USA

²⁸ Kavli Institute for Particle Astrophysics and Cosmology (KIPAC), Stanford, CA 94305, USA

²⁹ Department of Physics, California Institute of Technology, Pasadena, CA 91125, USA

³⁰ Physics and Astronomy Department, Stony Brook University, Stony Brook, NY 11794, USA

³¹ Instituto de Física, Pontificia Universidad Católica de Valparaíso, Casilla 4059, Valparaíso, Chile

³² School of Earth and Space Exploration, Arizona State University, Tempe, AZ 85287, USA

³³ NASA/Goddard Space Flight Center, Greenbelt, MD 20771, USA

³⁴ MIT Kavli Institute, Massachusetts Institute of Technology, 77 Massachusetts Avenue, McNair Building, Cambridge, MA 02139, USA

(Received March 14, 2022; Revised March 14, 2022; Accepted March 14, 2022)

Submitted to ApJ

ABSTRACT

The Sunyaev-Zel'dovich (SZ) effect introduces a specific distortion of the blackbody spectrum of the cosmic microwave background (CMB) radiation when it scatters off hot gas in clusters of galaxies. The frequency dependence of the distortion is only independent of the cluster redshift when the evolution of the CMB radiation is adiabatic. Using 370 clusters within the redshift range $0.07 \lesssim z \lesssim 1.4$ from the largest SZ-selected cluster sample to date from the Atacama Cosmology Telescope, we provide new constraints on the deviation of CMB temperature evolution from the standard model $\alpha = 0.017^{+0.029}_{-0.032}$, where $T(z) = T_0(1+z)^{1-\alpha}$. This result is consistent with no deviation from the standard adiabatic model. Combining it with previous, independent datasets we obtain a joint constraint of $\alpha = -0.001 \pm 0.012$.

Keywords: Cosmology (343); Cosmic microwave background radiation (322); Galaxy clusters (584); Sunyaev-Zeldovich effect(1654);

1. INTRODUCTION

The cosmic microwave background (CMB) is an almost-perfect blackbody with a temperature today of $T_0 = (2.72548 \pm 0.00057)$ K (Fixsen 2009). In the standard cosmological model, this radiation fills a universe characterized by a Friedmann–Lemaître–Robertson–Walker (FLRW) metric,

$$ds^2 = -c^2 dt^2 + a^2(t) d\mathbf{x}^2, \quad (1)$$

where $a = (1+z)^{-1}$ is the scale factor that describes the proper size of the spatial component \mathbf{x} . Under the assumption of adiabatic expansion—or, equivalently, conservation of the energy-momentum tensor—one can show that the radiation energy density $u \propto T^4$ scales as $u \propto a^{-4}$. Therefore, the associated radiation temperature must evolve as $T(z) = T_0(1+z)$. Empirically probing this temperature–redshift relation is thus a test of some of the most fundamental assumptions in cosmology. Deviations would indicate either that the FLRW metric does not describe our Universe or else that the CMB does not behave adiabatically. In the first case, the cosmological principle of homogeneity and isotropy would be violated. Though isotropy is well-established observationally, we could conceivably be at the centre of a large scale, isotropic inhomogeneity, such as a void (Goodman 1995; Clarkson 2012). In the other case of non-adiabaticity, energy would be injected into or removed from the CMB by exotic physics such as vacuum energy decay (Lima 1996; Lima et al. 2000; Jetzer et al. 2011). Finally, variation of fundamental constants such as the fine-structure constant can mimic non-adiabatic behavior in the observables from which $T(z)$ is reconstructed (e.g., de Martino et al. 2016).

It is customary to parameterize deviations from the expected evolution as (Lima et al. 2000):

$$T(z) = T_0(1+z)^{1-\alpha}. \quad (2)$$

Non-zero α indicates deviation from the standard cosmology. The parameterization of Equation 2 is motivated by the scenario in which the increase (or decrease) in photon number is ‘adiabatic’, i.e., in which the specific entropy of the CMB radiation remains constant (Lima et al. 2000). However, since α is small, a Taylor expansion of Equation 2 can be used to assess other models in the $z < \mathcal{O}(1)$ regime (Avgoustidis et al. 2016). Chluba (2014) observes that unless the energy spectrum of the injected/removed photons has a very particular form, this mechanism introduces distortions into the CMB blackbody spectrum that are already strongly constrained by the Cosmic Background Explorer (COBE) Far InfraRed Absolute Spectrophotometer (FIRAS; Fixsen 2009). Nevertheless, probing α still provides a valuable empirical check of the validity of our cosmological model. It not only serves as a ‘null test’ against the finely-tuned case in which adiabatic energy injection/removal causes no spectral distortions, but is also in principle sensitive to large scale inhomogeneity in the metric (see Chluba 2014).

Two methods have been used to directly probe $T(z)$. The first uses line spectroscopy of quasars to identify, for instance, the fine-structure line of C I or molecular rotational transitions of CO due to absorption of CMB radiation. Avgoustidis et al. (2016) combined the result from 10 quasar absorption line systems at $z = 0.89–3.025$ (Srianand et al. 2000; Ge et al. 2001; Molaro et al. 2002; Cui et al. 2005; Srianand et al. 2008; Noterdaeme et al. 2010, 2011; Muller et al. 2013) and provided a constraint of $\alpha = 0.005 \pm 0.022$. Recently, Klimenko et al. (2020) updated the line modeling by correcting for the collisional excitation of CO rotational transitions and obtained a constraint of $\alpha = -0.015^{+0.030}_{-0.028}$ from 12 systems. The second method, which we use in this paper, exploits the fact that the amount of inverse Thomson scattering of CMB photons in galaxy clusters, known as the Sunyaev-Zeldovich (SZ) effect (Zeldovich & Sunyaev

1969; Sunyaev & Zeldovich 1972), depends on $T(z)$. The scattering distorts the CMB blackbody spectrum to induce a frequency-dependent change in its intensity, or (as is more convenient to work with) its thermodynamic temperature:

$$\Delta T(\hat{r}, \nu) = T_0 \int dr n_e(\hat{r}, z) \sigma_T \left[f_{\text{SZ}}(\nu, T_e) \frac{k_B T_e}{m_e c^2} - \frac{v_r}{c} \right], \quad (3)$$

where the integral is done along the line of sight in direction \hat{r} , n_e is the number density of electrons, T_e is their temperature, v_r/c is the proper radial velocity of the cluster relative to the speed of light, k_B is the Boltzmann constant, m_e the mass of the electron, and σ_T is the Thomson cross section. The function $f_{\text{SZ}}(\nu, T_e)$ encodes the frequency dependence of the SZ effect. Normally, one makes the approximation that T_e is constant through the cluster to simplify the expression to:

$$\Delta T(\hat{r}) = T_0 \left[f(\nu, T_e) y_c(\hat{r}) - \tau \frac{v}{c} \right], \quad (4)$$

where y_c is the Compton parameter, proportional to the integrated gas pressure, $n_e T_e$, and τ is the integrated optical depth along the line of sight. The last term in Equation 4 is the kinematic SZ effect (kSZ) and has the same spectral shape as the CMB, whereas the former characterizes the thermal SZ (tSZ) effect and has the spectral shape

$$f(\nu) = x \coth(x/2) - 4, \quad x \equiv \frac{h\nu(1+z)}{k_B T(z)}, \quad (5)$$

in the non-relativistic approximation of small T_e ,¹ where h is the Planck constant. If $\alpha = 0$, then the $1+z$ in the numerator is cancelled out (see Equation 2) and $f(\nu)$ is independent of redshift. If, on the other hand, the temperature deviates from the canonical form, it can be probed by multi-frequency observations (Rephaeli 1980). For instance, the ratio of the SZ amplitude measured at two different frequencies, ν_1 and ν_2 , will depend on the redshift:

$$r(z) = \frac{f(\nu_1, z)}{f(\nu_2, z)}. \quad (6)$$

Measuring $r(z)$ over a range of redshifts can thus constrain α .

This technique was first used by Battistelli et al. (2002) using two clusters (Coma and Abell 2163) observed with multiple observatories at four frequencies between 30 and 270 GHz to measure an α consistent

¹ We investigate the effect of the full relativistic treatment on our result in §5.

with zero with a 2σ uncertainty of $\Delta\alpha \sim 0.3$. Since then, results using increasing numbers of clusters have found no evidence for non-zero α with shrinking uncertainties (all 1σ): Luzzi et al. (2009) analysed nine clusters using six frequencies between 30 and 353 GHz from multiple observatories and found $\Delta\alpha \sim 0.06\text{--}0.09$; Saro et al. (2014) used 158 clusters observed by the South Pole Telescope at 95 and 150 GHz to measure $\Delta\alpha = 0.03$; Hurier et al. (2014) used maps from the *Planck* satellite to analyze 813 clusters from the first catalog of *Planck* clusters (PSZ1) and reported $\Delta\alpha = 0.017$, while Luzzi et al. (2015) used a different pipeline on the same maps and 103 clusters from PSZ1, yielding $\Delta\alpha = 0.016$; de Martino et al. (2015), on the other hand, used 481 X-ray selected clusters from *ROSAT* to analyze the *Planck* data and measured $\Delta\alpha = 0.013$, but with a possible systematic of up to $\Delta\alpha = 0.02$ (with the sign being the same as that of α) coming from their map-cleaning process. Combining all the foregoing quasar and SZ data, a constraint of $\Delta\alpha = 0.013$ is achieved (Avgoustidis et al. 2016; Klimenko et al. 2020).²

In this paper, we provide an updated measurement of α with the largest catalog of SZ clusters from the Atacama Cosmology Telescope (ACT) out to a redshift of 1.4 (Section 2). This work improves on the likelihood analysis used in previous studies (Section 3) and validates it with simulations (Section 4). We also examined the potential systematics in the result, some of which have been neglected in similar analyses (Section 5).

2. DATA

We use the ACT DR5 maps (Naess et al. 2020) at 98 GHz and 150 GHz for this analysis.³ The data include both nighttime observations from 2008 to 2018 and daytime observations from 2014 to 2018, covering 18,000 deg² of the sky. Maps were made by co-adding individual, maximum-likelihood maps from each observation season and detector array. The final, convolved maps at 98 and 150 GHz have FWHM resolutions of 2.2' and 1.4', respectively.

2.1. SZ Sample and Photometry

Our SZ cluster sample comes from Hilton et al. (2021), which is the largest homogeneous SZ-selected catalog to date, containing 4,195 optically confirmed clusters within a search area of 13,211 deg². The sample selection in Hilton et al. (2021) assumes that the relative

² This is slightly larger than the corresponding value reported in (Avgoustidis et al. 2016), as we include the systematic error reported by de Martino et al. (2015).

³ DR5 maps and ancillary products are available at: https://lambda.gsfc.nasa.gov/product/act/actpol_prod_table.cfm

amplitude of the two bands follows the adiabatic model ($\alpha = 0$). We test in Section 4.2 that this does not bias our result towards a false negative.

SZ signals are measured with a matched-filter technique (Melin et al. 2006) in two steps. Cluster shapes and locations are extracted with a multi-band matched filter applied to each map at frequency ν_i :

$$\psi(\nu_i, \mathbf{k}) = \sum_j \mathbf{N}_{ij}^{-1}(\mathbf{k}) B_j(k) f_{\text{SZ}}(\nu_j) S(k, \nu_j), \quad (7)$$

where S is the Universal Pressure Profile (UPP) for galaxy clusters (Arnaud et al. 2010), B is the beam window function, and \mathbf{N}_{ij} is the noise covariance matrix that includes contributions from instrumental noise and non-tSZ sky signals. We estimate \mathbf{N}_{ij} as in Hilton et al. (2021), except that we update this method by doing two passes of filtering. After filtering the map once, we find all clusters with signal-to-noise ratio (S/N) > 5 , subtract them from the map, and use it as noise estimation for the second pass of filtering. This multi-band matched-filter is applied for 31 candidate profiles with projected angular size θ_{500c} (defined as the cluster radius enclosing an average density 500 times the critical density of the Universe at the cluster redshift) log-uniformly spaced from $0.6'$ to $8'$. The profile S that maximises the S/N for each cluster is then selected for signal extraction.⁴

Next, the SZ signal is measured in each band with spatial matched-filter forced photometry. This has been demonstrated to be robust against Galactic contamination and infrared emission from the galaxy clusters (Erler et al. 2018). We smooth the 150 GHz map down to the same angular resolution as the 98 GHz map ($2.2'$) with point spread function (PSF) matching, and filter both maps with the same Fourier kernel:

$$\psi_{98,150}(\mathbf{k}) = \mathbf{N}_{98}^{-1}(\mathbf{k}) B_{98}(k) S(k), \quad (8)$$

where S is the cluster profile determined from the multi-band matched filter as described above. Although the filter at 150 GHz is not the optimal matched filter, this technique ensures that the potential bias from a filter-mismatch is a multiplicative factor common to both frequencies that is marginalized over in the likelihood analysis (Section 9), and thus leaves the constraints on α unbiased (Saro et al. 2014).

2.2. Sample selection

A S/N threshold of $\xi = 5.5$ for the SZ signal measurement at each frequency is applied to eliminate samples that are more susceptible to systematics, such as primary CMB anisotropies or infrared/radio emission. This particular choice of S/N cut is conservative and is informed by simulations (see Section 4.1). However, it inevitably biases the signal towards higher values since positive fluctuations will be preferentially included. Because this bias will not necessarily be the same in both frequencies, it may not cancel out in the ratio between the two bands that we use in our analysis, and so we correct for it in our likelihood calculation (Section 3).

To eliminate potential contamination from bright radio sources, we exclude clusters found within $2'$ of sources brighter than 10 mJy in the NRAO VLA Sky Survey (NVSS, Condon et al. 1998) 1.4 GHz catalog, or sources brighter than 15 mJy in the Sydney University/Molonglo Sky Survey (SUMSS Mauch et al. 2003) 843 MHz catalog. The combination of these two catalogs covers the full survey region of ACT DR5. Assuming a synchrotron spectral index -0.7 in flux (Dicker et al., in prep.), this ensures the bias is below 3% for 99% of the sample at 98 and 150 GHz. Tests in Section 5 show that our result does not change when a stricter limit is applied.

The two individual selections remove 3627 and 929 clusters respectively, and leave our final sample with 370 clusters in a redshift range of $0.07 \lesssim z \lesssim 1.4$.

2.3. Band centers and calibration

The effective band center for the tSZ signal is obtained by integrating its spectrum over the detector bandpass. We ignore the change in the band center due to deviation of the standard tSZ spectrum for models with non-adiabatic temperature evolution, as the difference is negligible. However, the effective bandpasses can vary across the map due to different combinations of detectors being coadded in different regions. Following the prescription of Naess et al. (2020, Appendix A.4), we calculate the resulting effective bandpass centers in a $0.5^\circ \times 0.5^\circ$ grid,⁵ finding that the mean band centers for all clusters are 97.4 and 147.8 GHz, respectively, with a variation that translates to a 1% variation in the tSZ signal ratio between the two frequencies. We verified that this variation of band centers across the map does not change our final result. Due to uncertainties in the detector bandpass measurement, there is a $\sim 1.5/2.4$ GHz systematic shift in the band center estimate at 98/150 GHz respectively (Madhavacheril et al. 2020). This re-

⁴ We verified that 31 filters is sufficiently precise by performing the analysis on a subset of 12, sparsely-spaced profiles and finding consistent results.

⁵ The data products required for this are available at: https://lambda.gsfc.nasa.gov/product/act/actpol_dr5_aux_prod_get.cfm

sults in a 2% uncertainty in the tSZ signal ratio. Furthermore, the ACT DR5 maps are separately calibrated against *Planck* to the $\mathcal{O}(1\%)$ level (Naess et al. 2020). Assuming these uncertainties are independent at the two frequencies, the relative calibration uncertainty is $\mathcal{O}(1.5\%)$. Combining the two, we adopt a 2.5% prior

on the relative calibration between our two frequency channels to account for the instrumental uncertainties.

3. PARAMETER INFERENCE

Given the temperature evolution described in Equation 2, assuming Gaussian errors, and accounting for the S/N threshold ξ , the likelihood function is (e.g., Ivezić et al. 2014, §4.2.7):

$$\mathcal{L}_i(s_{i,98}, s_{i,150} | \alpha, \eta, \mu_{i,150}) = \frac{4}{2\pi\sigma_{i,98}\sigma_{i,150}} \frac{\exp\left[-\frac{(s_{i,98} - \eta r(\alpha, z_i) \mu_{i,150})^2}{2\sigma_{i,98}^2}\right]}{\text{erfc}\left[\frac{\xi\sigma_{i,98} - \eta r(\alpha, z_i) \mu_{i,150}}{\sqrt{2}\sigma_{i,98}}\right]} \frac{\exp\left[-\frac{(s_{i,150} - \mu_{i,150})^2}{2\sigma_{i,150}^2}\right]}{\text{erfc}\left[\frac{\xi\sigma_{i,150} - \mu_{i,150}}{\sqrt{2}\sigma_{i,150}}\right]}, \quad (9)$$

where s_i are the measured tSZ signals, and the uncertainties σ are taken as known quantities, which are taken to be independent between two frequencies for each cluster. We note that this is a simplification since the primary CMB anisotropy and astrophysical emission introduce correlated errors in the tSZ signal estimation even though the instrumental noise could be treated as independent. This correlation is accounted for in Section 5 and is found to be insignificant in altering the result. We parameterize the fitting model with the amplitude of the tSZ signal at 150 GHz, $\mu_{i,150}$, and the ratio between the signals in the two bands, $r(\alpha, z_i) \equiv \mu_{i,98}/\mu_{i,150}$ (Equation 6). The parameter η accounts for any relative calibration difference between the two bands (c.f., Luzzi et al. 2009) and is marginalized over in our results. As discussed in Section 2.3, we use a Gaussian prior with 2.5% standard deviation for η . Finally, the probability distribution functions of $s_{i,98}$ and $s_{i,150}$ are truncated to 0 below the S/N threshold ξ , and the complementary error functions in the denominator account for their normalization. When the value of $\mu_{i,150}/\sigma_{i,150}$ (or, for 98 GHz, $\eta r \mu_{i,150}/\sigma_{i,98}$) is well above the threshold (e.g., $\gtrsim \xi + 2$), the complementary error function approaches an asymptotic value of 2 and the likelihood reduces to the standard Gaussian form. We note that Saro et al. (2014) and de Martino et al. (2015) do not account for this effect, which could in principle bias α , but would depend on the S/N distribution of their samples.

The free parameters in the model are $\{\alpha, \eta, \mu_{i,150}\}$. For 370 clusters, the total number of parameters is thus 372. The model amplitudes $\mu_{i,150}$ are essentially nuisance parameters over which we integrate, assuming flat prior distributions, to obtain the marginalized posterior distributions of α and η :

$$\log \mathcal{P}(\alpha, \eta) = \sum_i \log \int \mathcal{L}_i(s_{i,98}, s_{i,150} | \alpha, \eta, \mu_{i,150}) d\mu_{i,150}. \quad (10)$$

For the final estimation of α , we report the mean of the posterior distribution after marginalizing over η in Equation 10. Since the individual likelihood function for each cluster in Equation 9 is non-Gaussian and the high dimensionality of the problem could lead to a volume effect such that the posterior mean might be offset from the maximum *a posteriori* (MAP) value, we also report the MAP values for reference. They are calculated by maximizing

$$\log \mathcal{L}_{\text{ML}}(\alpha, \eta) = \sum_i \log \mathcal{L}_i(s_{i,98}, s_{i,150} | \alpha, \eta, \hat{\mu}_{i,150}), \quad (11)$$

where $\hat{\mu}(\alpha, \eta)_{i,150}$ is the maximum-likelihood estimate of $\mu_{i,150}$ for a given α , determined by:

$$\partial_{\mu_{i,150}} \mathcal{L}_i(s_{i,98}, s_{i,150} | \alpha, \eta, \mu_{i,150}) \Big|_{\hat{\mu}_{i,150}} \equiv 0. \quad (12)$$

When the selection bias correction is ignored, Equation 11 reduces to the form that is used by Saro et al. (2014) as the likelihood function (their Equation 5). However, we note that this is merely a cross section of the true multivariate likelihood function (Equation 10) that fixes all the nuisance parameters at their maximum-likelihood values. While its peak value can be used for MAP estimation, the quantile range of this distribution does not include the covariances with $\{\mu_{i,150}\}$, and is an underestimation of the true uncertainty. For our MAP estimation, we quote the standard deviation of the marginalized posterior distribution as the 1σ uncertainty.

We use a Markov-chain Monte Carlo sampler (`emcee`, Foreman-Mackey et al. 2013) to find the posterior distribution of Equation 10 and the maximum-likelihood solution to Equation 11. To ensure convergence of the MCMC, we compute the maximum autocorrelation of the chains, which we find to be $T = 30$ iterations, and discard the first $7T$ iterations from our results (see Foreman-Mackey et al. 2013).⁶

4. SIMULATIONS

4.1. *WebSky* simulation

To validate the method outlined above, we applied it to simulated ACT observations using inputs from *WebSky* (Stein et al. 2020). This simulation of the cosmic web at millimeter wavelengths includes the CMB, the cosmic infrared background (CIB) and the SZ effect. The AGN feedback effect on the cluster pressure profile is also considered in the simulation with a prescription from Battaglia et al. (2012). By mixing different components from the *WebSky* maps, we are able to simulate two scenarios: first, a sky with only the CMB and the tSZ signals with $\alpha = 0$, and second, a sky that also includes the CIB and the kSZ effect. We add ACT DR5 white noise realizations to the simulations, as realizations of ACT’s more complex noise properties (Naess et al. 2020) are not available. However, we are looking at small scales where the white noise approximation should suffice for the purposes of testing how the different signal components affect our method.⁷ The cluster extraction and photometry pipelines are the same as used in the analysis of real data.

A positive correlation between the CIB and the cluster tSZ signal is expected (Addison et al. 2012) and has been observed by various experiments (Dunkley et al. 2013; George et al. 2015; Planck Collaboration et al. 2016). As infrared emission from dust-obscured star formation peaks in the redshift range $1 \lesssim z \lesssim 2$, its correlation with the tSZ signal is most significant at the higher end of the redshift distribution of our sample (e.g., Addison et al. 2012; Madau & Dickinson 2014). For most of the sources close to the center of the matched filter, this contamination acts as a negative bias to the tSZ decrement measurement (but due to the ringing of the filter, the infill could also lead to a positive bias for sources in

⁶ We have also run the MCMC for our baseline sample of clusters to over 2,500 iterations and confirmed that this autocorrelation length is stable and that having a longer burn-in period does not alter our results.

⁷ Using white noise can overestimate the cluster S/N, as noted by (Hilton et al. 2021) who also used this approximation, but we verify that our results are robust against higher S/N cuts (Section 5).

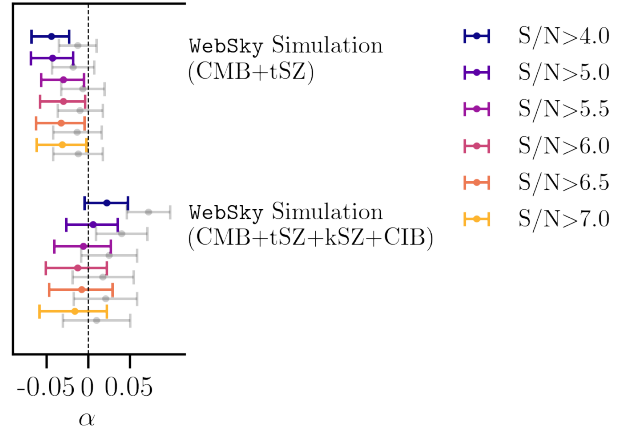


Figure 1. Constraints on α from *WebSky* simulations with input $\alpha = 0$. The colored points indicate the mean of the marginalized posterior distributions with 1σ error bars. The grey points indicate the MAP value with the same error bars as the colored ones. Based on the CMB+tSZ+kSZ+CIB simulation results, we restrict the analysis to data with $S/N > 5.5$ to avoid contamination from infrared sources.

the intermediate radii from the center; Dicker et al., in prep.), and has more impact on the 150 GHz band and thus translates into a positive bias in α .

We perform the analysis with various S/N cuts ξ in each band, and report in Figure 1 the posterior mean (in colors) and MAP (in grey) estimation of α as described in Section 3. For this realization, posterior mean and MAP estimation are offset by $\sim 1\sigma$, which could be related to the volume effect.

For the *WebSky* simulation that includes CMB+tSZ, our result is consistent with $\alpha = 0$ for all S/N selection within 68% credible intervals. This also demonstrates that using a fixed UPP profile for signal estimation is sufficient for our uncertainty, despite the fact that the tSZ profile might have redshift dependency due to feedback. Although the posterior mean and MAP are offset from each other, their trends are similar as the S/N is varied. Figure 1 indicates that the inclusion of the CIB component may introduce positive bias in α at $\xi \lesssim 5$. This bias appears to be mitigated by choosing clusters with higher S/N, as those clusters are more tSZ-dominated, massive clusters. Guided by this test, we adopt $\xi = 5.5$ in our analysis. We verify in Section 5 that our result is insensitive to the choice of S/N threshold beyond 5.5.

In the validation of our method described in this section we are limited by having only one *WebSky* realization. We did a simple check by reversing the coordinates of the clusters in the map (flipping them both north-south and east-west), thereby changing the S/N distri-

bution of the sample. In this case, the difference between the CMB+tSZ and CMB+tSZ+kSZ+CIB posteriors is little larger (but $\lesssim 1\sigma$), and the positive bias in α at $\xi \lesssim 5$ is less apparent. However, we find broad agreement with the results above; and we retain the $\xi = 5.5$ threshold out of caution for the possible effect of the CIB.

4.2. Pseudo-simulation

We further validate our pipeline with a suite of pseudo-simulations. For these simulations, we insert UPP-model clusters into maps containing a CMB realization and white noise that follows the ACT DR5 inverse variance maps. The mock cluster sample is drawn from the [Tinker et al. \(2008\)](#) halo mass function, assuming a modified version of the [Arnaud et al. \(2010\)](#) SZ-mass-scaling relation, with the normalization adjusted to approximately reproduce the number of clusters that are observed in the real maps. This test simulates the effect of a non-standard temperature evolution by setting the injected SZ signal at the two observing frequencies according to specified values of α . As all clusters are selected with a multi-frequency matched-filter assuming the standard adiabatic model ([Hilton et al. 2021](#)), this test is crucial to preclude the possibility of a false-negative non-detection of the deviation.

We use three inputs for the temperature evolution, $\alpha = 0, -0.1$, and 0.05 , and generate ten pseudo-catalogs for each of these inputs. Similar to [Hilton et al. \(2021\)](#), we search for clusters using the multi-frequency matched filter assuming $\alpha = 0$ with detection threshold $\xi = 4$, and perform the forced photometry as outlined above using selection $\xi = 5.5$. Without applying the prior on η and using ACT beam profile for simulation, the posterior mean agrees with $\eta = 1$ in all three cases, but the recovered η is biased by 0.01 (at the 3σ level according to the error on the mean of the 10 simulations) if we use a Gaussian beam profile with similar beam size. This is likely due to the imperfect PSF matching we used when smoothing the 150 GHz maps to the same scale as 98 GHz maps in the Gaussian case. While we don't find a similar offset when using the ACT PSF, out of an abundance of caution, we choose to augment the 2.5% prior width based on instrument calibration and bandpass (Section 2.3) by an uncorrelated 1% uncertainty. Using the updated 2.7% prior on η , we find that the recovered α still agrees with the inputs, with average (over 10 simulations) $\alpha = -0.004 \pm 0.006, -0.102 \pm 0.007$ and 0.047 ± 0.005 , respectively. This test verifies that our pipeline is not preferentially selecting clusters that appear, by chance, close to $\alpha = 0$. A similar conclusion was also reached by [Saro et al. \(2014\)](#).

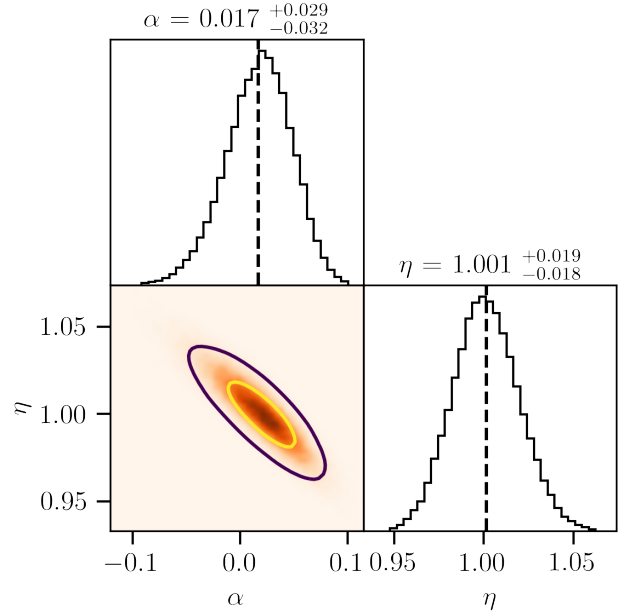


Figure 2. The posterior distribution of α and η after marginalizing over nuisance parameters $\{\mu_{i,150}\}$. The contours mark 68 and 95% confidence intervals in the marginalized 2D space. Reported uncertainties are derived from the 68% quantile of the marginalized 1D distributions.

5. RESULTS

Figure 2 shows the marginalized posterior distribution for α and η . Using the mean of the marginalized posterior distribution, we report the following constraint on the CMB temperature evolution:

$$\alpha = 0.017^{+0.029}_{-0.032}. \quad (13)$$

This is fully consistent with no deviation from the adiabatic evolution. In addition to the posterior mean value we quote as baseline result, we also report the MAP estimation $\alpha = 0.032 \pm 0.030$ (where the error bar is the 68% credible interval of the posterior distribution), which is also consistent with the standard temperature evolution model within $\sim 1\sigma$. Since the estimate of α is highly degenerate with the relative calibration η , the result is sensitive to the assumed prior on η . Lifting this prior constraint we find $\alpha = 0.013 \pm 0.040$ and $\eta = 1.004 \pm 0.026$, consistent with baseline result. The comparison of these results are summarized in Figure 3.

In Figure 4 we show our result next to previous results obtained from SZ measurements of clusters from SPT ([Saro et al. 2014](#)) and *Planck* ([Hurier et al. 2014; de Martino et al. 2015; Luzzi et al. 2015](#)), and from quasar absorption lines ([Muller et al. 2013; Klimenko et al. 2020](#)). The uncertainty in our measurement is comparable to [Saro et al. \(2014\)](#) which used a similar

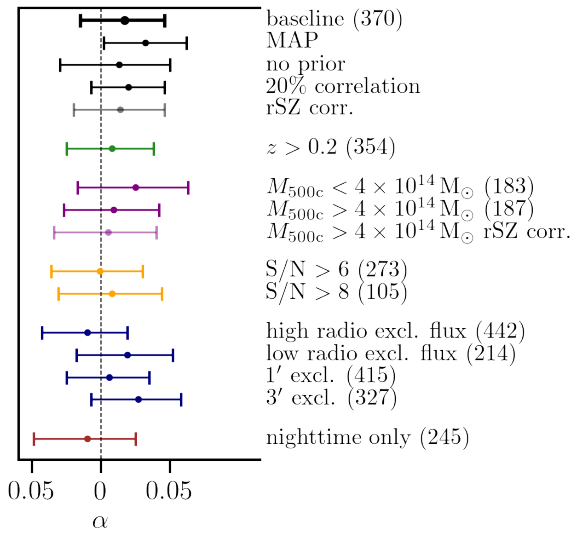


Figure 3. The point estimation for α (posterior mean, except for the second row that reports MAP) with the associated 68% credible interval derived from the posterior distribution after marginalizing over all nuisance parameters. Numbers in parentheses indicate how many clusters were included in each test. The top, black point is our baseline result with the selection criteria detailed in the main text. Colored lines denote various systematics checks (see text for details). From top to bottom, these are tests for: the cluster redshift and completeness (green), the cluster mass and relativistic correction (purple), the S/N selection bias (orange), contamination from radio sources (blue) and systematics associated with day-time data (brown).

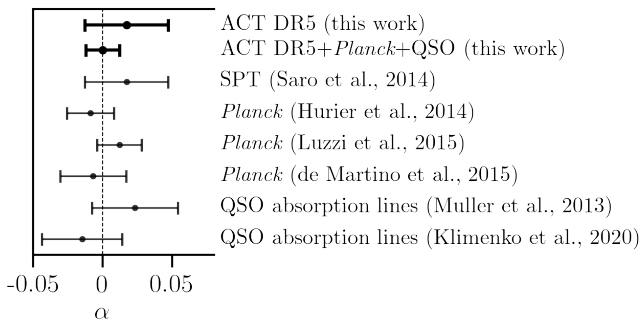


Figure 4. Constraints on α from tSZ measurements and quasar absorption line studies. The result combining ACT, *Planck* (except for Luzzi et al. 2015; see text), and quasar absorption lines (Muller et al. 2013; Klimenko et al. 2020) is shown in the second row.

two-frequency observation, despite the improvement in statistical errors from the larger sample with higher S/N threshold. This is because our total error is dominated by the two sources of uncertainty in addition to the statistical uncertainties that we account for in our likelihood analysis. The first, and biggest, of these comes from the uncertainty of the relative calibration of our two frequency bands, parameterized by η in our likelihood (Equation 9, Luzzi et al. 2009). We note that this has not been explicitly marginalized over in some previous studies (Saro et al. 2014; de Martino et al. 2015). The second source of uncertainty comes from covariance with the nuisance parameters $\{\mu_{i,150}\}$ that we marginalize over. This factor, which is not included in the analysis of Saro et al. (2014), makes up about 10% of our uncertainty budget.

The constraint on α can be improved by combining the results derived from independent data sets in an inverse variance weighted average. Our analysis has been done on a sub-sample of 310 clusters above redshift 0.3 that does not overlap with PSZ1 (Planck Collaboration et al. 2015). Combining the α constraint from this sample with those derived using 481 clusters with $z < 0.3$ from the X-ray selected *Planck* sample (de Martino et al. 2015), using 267 clusters from a *Planck* SZ-selected sample above $z = 0.3$ (Hurier et al. 2014; Avgoustidis et al. 2016), and using the quasar absorption line studies (Muller et al. 2013; Klimenko et al. 2020), we find a joint constraint of $\alpha = -0.001 \pm 0.012$, assuming independent Gaussian errors in each result. The individual datasets used for the combination are also shown in Figure 5. We exclude other results from this combination because they do not indicate their cluster catalog explicitly and we wish to avoid overlap with our sample; the statistical improvement by including them would be marginal.

We performed a battery of tests to examine the impact of other potential systematics not accounted for in our formalism. A summary of the results from these tests, which we describe below, is shown in Figure 3.

Correlated error—As mentioned in Section 3, correlated astrophysical sources would cause correlated errors in the measurement at two frequencies. To test this effect, we modified the likelihood function in Equation 9 by introducing the Pearson Product-Moment correlation factor $\rho = 0.2$ for all clusters (Orlowski-Scherer et al. 2021). The two individual Gaussian functions in the numerator are replaced with the 2D Gaussian function and the complementary error function are replaced with the 2D integrals to account for the adjusted normalization. The computational cost for evaluating this generalized likelihood function is increased significantly. Therefore, we directly sample the 2D marginalized likelihood of $\{\alpha, \eta\}$ with a Gaussian process emulation technique (Pellejero-Ibanez et al. 2020) using the GPy package (GPy since

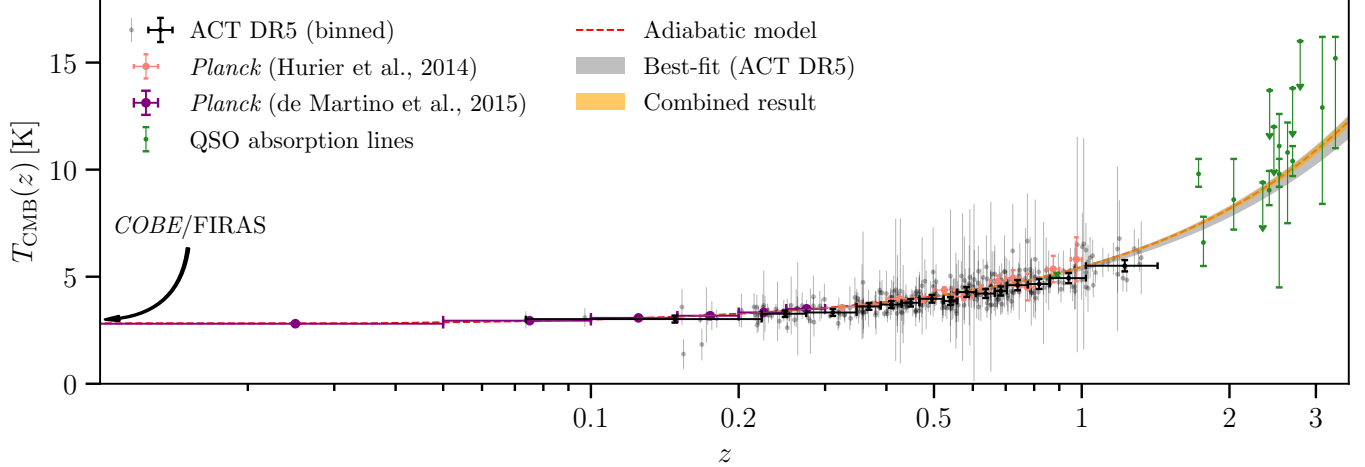


Figure 5. CMB temperature estimation inferred from each of the 370 clusters in the sample by inverting the likelihood function Equation 9 (grey bars). The error bar of each point is the 68% confidence interval for each \mathcal{L}_i . For visualization purpose, we bin our measurements in redshift and show them as black error bars. This binning is arbitrary and is not used for our analysis. We also include results from two independent analyses of *Planck* clusters, which estimated the redshift-bin-averaged temperature measurements (Hurier et al. 2014; de Martino et al. 2015), and from quasar absorption line studies (Muller et al. 2013; Klimenko et al. 2020). The dashed line marks the standard adiabatic evolution of $T(z)$. The shaded grey region is our best-fit constraint and is consistent with the adiabatic model to within its uncertainty of $\Delta\alpha = 0.03$. The shaded orange region marks the combined constraints with uncertainty of $\Delta\alpha = 0.012$.

2012).⁸ The result is $0.020^{+0.026}_{-0.027}$, consistent with the baseline result and with a 10% improvement in the constraining power. Since the simulation pipelines we have used to validate our methods do not implement this novel fitting procedure, we do not use it for our baseline result, but future studies could benefit from using this treatment from end to end.

Completeness—Simulations with mock cluster catalogs indicate that the completeness of the ACT DR5 cluster sample drops at redshifts below 0.2 (Hilton et al. 2021). To check the potential impact from this redshift-dependent selection, we performed the analysis on a subsample of clusters with $z > 0.2$, where there is a roughly uniform 90% completeness for cluster mass $M_{500c} > 3 \times 10^{14} M_\odot$,⁹ and obtained a consistent result.

Cluster mass—We checked the dependence of our result on cluster mass (assuming the mass-scaling relation from Arnaud et al. 2010) by performing the analysis on subsets of clusters with mass M_{500c} above and below $4 \times 10^{14} M_\odot$. The low-mass sample shows a slightly larger deviation from $\alpha = 0$, which could be related to

the higher contamination from the infrared emission as the tSZ S/N is typically lower for this sample. The massive clusters are expected to have a higher relativistic SZ (rSZ) correction due to their higher virial temperatures, and one might therefore anticipate that the rSZ effect could masquerade as a non-zero α . Using the mass-temperature scaling relation from Arnaud et al. (2005) and the rSZ model up to the fourth term in temperature from Itoh et al. (1998), we correct for the rSZ effect for the high-mass and the baseline sample, and find little change in α (light purple and grey points in Figure 3).

Infrared Emission—Infrared emission from dusty, star-forming galaxies within the clusters could be biasing the tSZ signal measurement. However, our ability to perform an adequate component separation is limited by the frequency coverage. Our matched-filter-based photometry helps alleviate this bias as the infrared emission of the dusty galaxies in the cluster is more extended than the tSZ signal (Planck Collaboration et al. 2016). Additionally, Orlowski-Scherer et al. (2021) found that the ACT cluster sample does not, on average, show evidence for infrared emission after stacking the clusters on ACT 224 GHz or *Herschel* observations (albeit using a sample drawn from a smaller region than is covered by the DR5 maps; see Valiante et al. 2016; Smith et al. 2017). As discussed in Section 4.1, the positive bias in α could be further reduced by raising the S/N threshold for cluster selection. We run our fits with several higher S/N

⁸ <http://sheffieldml.github.io/GPy/>

⁹ Similar to θ_{500c} defined above, M_{500c} is the mass enclosed within a radius where the density is more than 500 times the critical density of the Universe. We estimate it from the SZ-mass scaling relation as in Hilton et al. (2021)

thresholds, shown in Figure 3, and find the result insensitive to the choice of threshold. This demonstrates that the threshold $\xi > 5.5$ is sufficient for reducing the infrared emission, in agreement with the results from the `Websky` simulation. Nevertheless, a sub- 1σ , positive bias due to the CIB could still be present (Section 4.1).

Radio Emission—Recently Orlowski-Scherer et al. (2021) and Dicker et al., (in prep.) have shown evidence that the radio point sources could be contaminating the tSZ signal measurement. However, it is hard to directly correct for it using low frequency surveys due to the spread in the sources’ spectral indexes. To guard against the radio emission from cluster-member galaxies biasing tSZ signal measurements, we removed clusters within $2'$ of radio sources in the joint NVSS and SUMSS catalog with flux density above certain thresholds (see Section 2.2). To test whether this selection is effective at rendering radio contamination negligible, we raise the flux threshold by a factor of 2 (i.e. relax the exclusion criteria) to select a sample that is potentially more contaminated by radio emissions, and then remove the flux threshold to obtain a sample that is less contaminated. Due to the ringing of the matched filters, sources at intermediate radii from the center of the cluster could negatively bias the tSZ decrement (for a $2.4'$ filter, this negative infill happens between $2'-4'$: Dicker et al., in prep.). In our case, we use matched filters with a variety of scales, with the majority of cluster photometry extracted using scales within $2'-4'$. To test the effect of the radio source infill at different distances, we alter the exclusion radius ($1'$ and $3'$) for the source cut while keeping the baseline flux threshold. The results are shown as blue bars in Figure 3. A $\sim 0.5\sigma$ shift of α in the negative direction occurs when more clusters with potential radio sources association are included. Nevertheless, the result is consistent within uncertainties, and we note that the best-fit α barely changes when the more aggressive cut is used. This indicates that the baseline cut is sufficient for removing radio contamination.

Nighttime-only Data—Our SZ measurements derive additional precision from daytime data that are included in ACT DR5 maps (Hilton et al. 2021). However, time-dependent beam deformations and, to a lesser extent, pointing offsets, both of which are due to the Sun heating the telescope structure, are not fully measured and corrected for in DR5 maps (Naess et al. 2020). We therefore perform the same analysis on maps made from nighttime-only data as a consistency test. The result, as shown in Figure 3, is consistent with the baseline constraint. It is worth noting that this split is also correlated with the high-mass splits as low-mass clusters

are hardly detected in this noisier map with same S/N threshold $\xi = 5.5$.

6. CONCLUSIONS

Using ACT DR5 data, we have measured the tSZ decrement at 98 and 150 GHz for 370 galaxy clusters in the redshift range $0.07 < z < 1.4$ using a matched-filter technique. We find that the tSZ signal ratio between the two bands is consistent with the CMB temperature evolution in the standard Λ CDM cosmological model. For a temperature evolution parametrized as $T(z) = T_0(1+z)^{1-\alpha}$ (Lima et al. 2000), we place a constraint, $\alpha = 0.017^{+0.029}_{-0.032}$ (or alternatively, $\alpha = 0.032 \pm 0.030$ for the MAP value) on the potential deviation from the adiabatic evolution using ACT data alone. This measurement is comparable to the most recent results based on other tSZ data (Saro et al. 2014; Hurier et al. 2014; de Martino et al. 2015; Luzzi et al. 2015). In obtaining this result, we refined the likelihood analysis from previous studies, and the robustness of this approach has been demonstrated with simulations. Combining this with previous results from independent data (de Martino et al. 2015; Hurier et al. 2014; Muller et al. 2013; Klimenko et al. 2020), we report an updated composite measurement of $\alpha = -0.001 \pm 0.012$.

Current constraining power using galaxy clusters observed by ACT is mainly limited by the degeneracy with the relative calibration factor (including the bandpass uncertainties) between two bands. This should be improved with wide-frequency-coverage data from future data releases from ACT and the Simons Observatory (Ade et al. 2019). Their higher frequency channels will also enable better cleaning of the infrared emissions, a major source of systematic uncertainty in the tSZ photometry at high redshifts.

ACKNOWLEDGMENTS

ACT was supported by the U.S. National Science Foundation through awards AST-0408698, AST-0965625, and AST-1440226 for the ACT project, as well as awards PHY-0355328, PHY-0855887 and PHY-1214379. Funding was also provided by Princeton University, the University of Pennsylvania, and a Canada Foundation for Innovation (CFI) award to UBC. ACT operates in the Parque Astronómico Atacama in northern Chile under the auspices of the Chilean National Agency for Research and Development (ANID). The development of multichroic detectors and lenses was supported by NASA grants NNX13AE56G and NNX14AB58G. Detector research at NIST was supported by the NIST Innovations in Measurement Science program.

Computations were performed on Hippo at the University of KwaZulu-Natal; data products used in this work also relied on computations on Cori at NERSC as part of the CMB Community allocation, on the Niagara supercomputer at the SciNet HPC Consortium, and on Feynman and Tiger at Princeton Research Computing. SciNet is funded by the CFI under the auspices of Compute Canada, the Government of Ontario, the Ontario Research Fund–Research Excellence, and the University of Toronto.

ADH is grateful for support from the Sutton Family Chair in Science, Christianity and Cultures. RH acknowledges funding from the NSERC Discovery Grants program, CIFAR Azrieli Global Scholars program and

the Alfred P. Sloan Foundation. KM and MH acknowledge support from the National Research Foundation of South Africa (grant number 112132). NS acknowledges support from NSF (grant number AST-1907657). CS acknowledges support from the Agencia Nacional de Investigación y Desarrollo (ANID) under FONDECYT (grant number 11191125). ZX is supported by the Gordon and Betty Moore Foundation.

Software: Astropy (Astropy Collaboration et al. 2013), NumPy (van der Walt et al. 2011), SciPy (Virtanen et al. 2020) Matplotlib (Hunter 2007), Cython (Behnel et al. 2011), emcee (Foreman-Mackey et al. 2013), GPy(GPy since 2012) .

REFERENCES

Addison, G. E., Dunkley, J., & Spergel, D. N. 2012, *MNRAS*, 427, 1741

Ade, P., Aguirre, J., Ahmed, Z., et al. 2019, *JCAP*, 2019, 056

Arnaud, M., Pointecouteau, E., & Pratt, G. W. 2005, *A&A*, 441, 893

Arnaud, M., Pratt, G. W., Piffaretti, R., et al. 2010, *A&A*, 517, A92

Astropy Collaboration, Robitaille, T. P., Tollerud, E. J., et al. 2013, *A&A*, 558, A33

Avgoustidis, A., Génova-Santos, R. T., Luzzi, G., & Martins, C. J. A. P. 2016, *PhRvD*, 93, 043521

Battaglia, N., Bond, J. R., Pfrommer, C., & Sievers, J. L. 2012, *ApJ*, 758, 75

Battistelli, E. S., De Petris, M., Lamagna, L., et al. 2002, *ApJL*, 580, L101

Behnel, S., Bradshaw, R., Citro, C., et al. 2011, *Computing in Science and Engineering*, 13, 31

Chluba, J. 2014, *MNRAS*, 443, 1881

Clarkson, C. 2012, *Comptes Rendus Physique*, 13, 682

Condon, J. J., Cotton, W. D., Greisen, E. W., et al. 1998, *AJ*, 115, 1693

Cui, J., Bechtold, J., Ge, J., & Meyer, D. M. 2005, *ApJ*, 633, 649

de Martino, I., Génova-Santos, R., Atrio-Barandela, F., et al. 2015, *ApJ*, 808, 128

de Martino, I., Martins, C. J. A. P., Ebeling, H., & Kocevski, D. 2016, *PhRvD*, 94, 083008

Dunkley, J., Calabrese, E., Sievers, J., et al. 2013, *JCAP*, 2013, 025

Erler, J., Basu, K., Chluba, J., & Bertoldi, F. 2018, *MNRAS*, 476, 3360

Fixsen, D. J. 2009, *ApJ*, 707, 916

Foreman-Mackey, D., Hogg, D. W., Lang, D., & Goodman, J. 2013, *PASP*, 125, 306

Ge, J., Bechtold, J., & Kulkarni, V. P. 2001, *ApJL*, 547, L1

George, E. M., Reichardt, C. L., Aird, K. A., et al. 2015, *ApJ*, 799, 177

Goodman, J. 1995, *PhRvD*, 52, 1821

GPy. since 2012, GPy: A Gaussian process framework in python, <http://github.com/SheffieldML/GPy>

Hilton, M., Sifón, C., Næss, S., et al. 2021, *ApJS*, 253, 3

Hunter, J. D. 2007, *Computing in Science and Engineering*, 9, 90

Hurier, G., Aghanim, N., Douspis, M., & Pointecouteau, E. 2014, *A&A*, 561, A143

Itoh, N., Kohyama, Y., & Nozawa, S. 1998, *ApJ*, 502, 7

Ivezić, Ž., Connolly, A. J., VanderPlas, J. T., & Gray, A. 2014, *Statistics, Data Mining, and Machine Learning in Astronomy* (Princeton, NJ: Princeton University Press)

Jetzer, P., Puy, D., Signore, M., & Tortora, C. 2011, *General Relativity and Gravitation*, 43, 1083

Klimenko, V. V., Ivanchik, A. V., Petitjean, P., Noterdaeme, P., & Srianand, R. 2020, *Astronomy Letters*, 46, 46

Lima, J. A. S. 1996, *PhRvD*, 54, 2571

Lima, J. A. S., Silva, A. I., & Viegas, S. M. 2000, *MNRAS*, 312, 747

Luzzi, G., Génova-Santos, R. T., Martins, C. J. A. P., De Petris, M., & Lamagna, L. 2015, *JCAP*, 2015, 011

Luzzi, G., Shimon, M., Lamagna, L., et al. 2009, *ApJ*, 705, 1122

Madau, P. & Dickinson, M. 2014, *ARA&A*, 52, 415

Madhavacheril, M. S., Hill, J. C., Næss, S., et al. 2020, *PhRvD*, 102, 023534

Mauch, T., Murphy, T., Buttery, H. J., et al. 2003, *MNRAS*, 342, 1117

Melin, J. B., Bartlett, J. G., & Delabrouille, J. 2006, *A&A*, **459**, 341

Molaro, P., Levshakov, S. A., Dessauges-Zavadsky, M., & D'Odorico, S. 2002, *A&A*, **381**, L64

Muller, S., Beelen, A., Black, J. H., et al. 2013, *A&A*, **551**, A109

Naess, S., Aiola, S., Austermann, J. E., et al. 2020, *JCAP*, **2020**, 046

Noterdaeme, P., Petitjean, P., Ledoux, C., et al. 2010, *A&A*, **523**, A80

Noterdaeme, P., Petitjean, P., Srianand, R., Ledoux, C., & López, S. 2011, *A&A*, **526**, L7

Orlowski-Scherer, J., Di Mascolo, L., Bhandarkar, T., et al. 2021, arXiv e-prints, arXiv:2105.00068

Pellejero-Ibanez, M., Angulo, R. E., Aricó, G., et al. 2020, *MNRAS*, **499**, 5257

Planck Collaboration, Ade, P. A. R., Aghanim, N., et al. 2015, *A&A*, **581**, A14

Planck Collaboration, Ade, P. A. R., Aghanim, N., et al. 2016, *A&A*, **594**, A23

Rephaeli, Y. 1980, *ApJ*, **241**, 858

Saro, A., Liu, J., Mohr, J. J., et al. 2014, *MNRAS*, **440**, 2610

Smith, M. W. L., Ibar, E., Maddox, S. J., et al. 2017, *ApJS*, **233**, 26

Srianand, R., Noterdaeme, P., Ledoux, C., & Petitjean, P. 2008, *A&A*, **482**, L39

Srianand, R., Petitjean, P., & Ledoux, C. 2000, *Nature*, **408**, 931

Stein, G., Alvarez, M. A., Bond, J. R., van Engelen, A., & Battaglia, N. 2020, *JCAP*, **2020**, 012

Sunyaev, R. A. & Zeldovich, Y. B. 1972, *Comments on Astrophysics and Space Physics*, **4**, 173

Tinker, J., Kravtsov, A. V., Klypin, A., et al. 2008, *ApJ*, **688**, 709

Valiante, E., Smith, M. W. L., Eales, S., et al. 2016, *MNRAS*, **462**, 3146

van der Walt, S., Colbert, S. C., & Varoquaux, G. 2011, *Computing in Science and Engineering*, **13**, 22

Virtanen, P., Gommers, R., Oliphant, T. E., et al. 2020, *Nature Methods*, **17**, 261

Zeldovich, Y. B. & Sunyaev, R. A. 1969, *Ap&SS*, **4**, 301